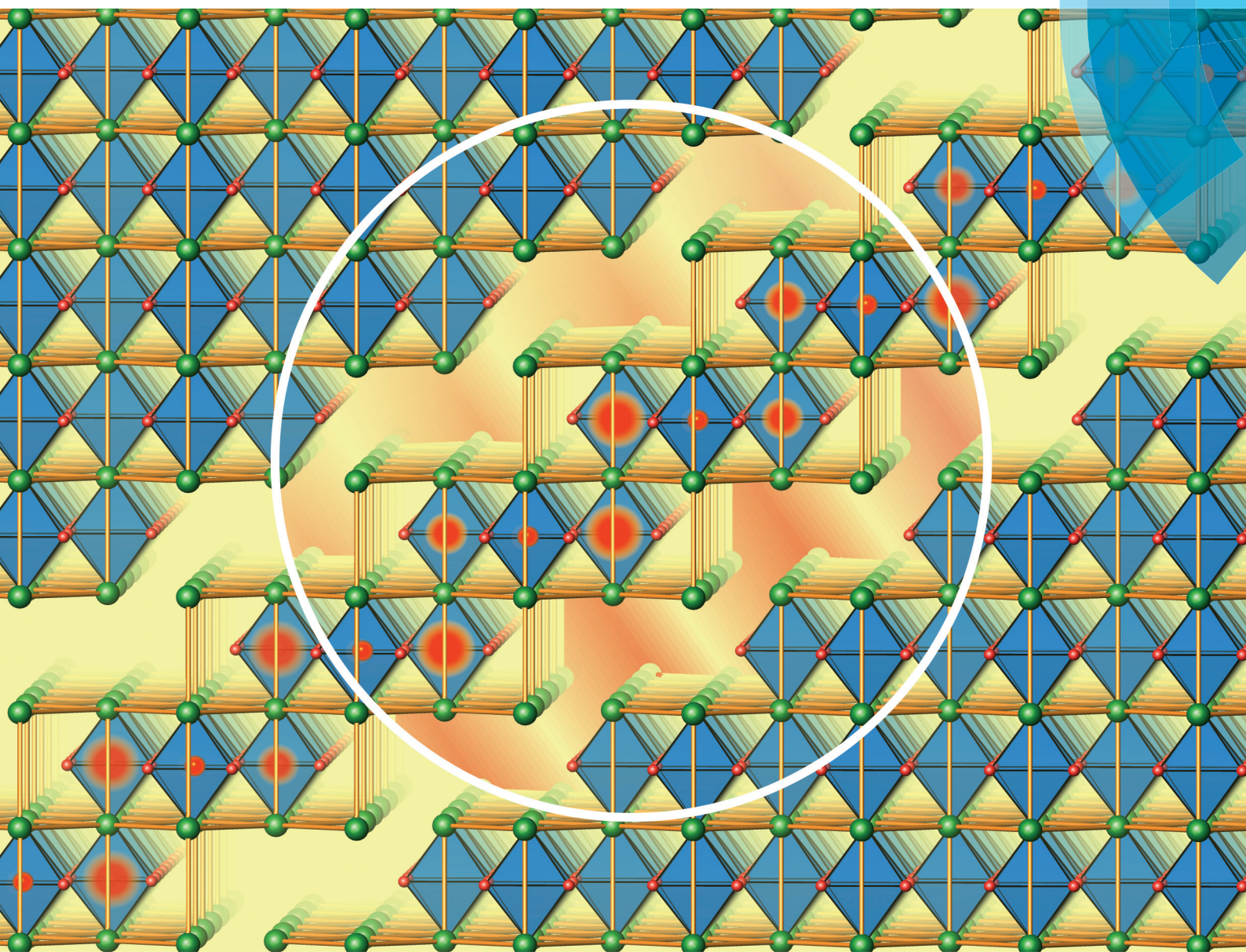


Dalton Transactions

An international journal of inorganic chemistry

rsc.li/dalton



ISSN 1477-9226



PAPER

Martin Jansen *et al.*

$\text{Sr}_5\text{Os}_3\text{O}_{13}$: a mixed valence osmium(v,vi) layered perovskite variant exhibiting temperature dependent charge distribution



Cite this: *Dalton Trans.*, 2018, **47**, 5968

Sr₅Os₃O₁₃: a mixed valence osmium(v,vI) layered perovskite variant exhibiting temperature dependent charge distribution†

Shrikant A. Mohitkar,^a Jürgen Nuss,^b Henning A. Höpfe,^c Claudia Felser^a and Martin Jansen^{*a,b}

New Sr₅Os₃O₁₃, as synthesized from binary constituents, exhibits several uncommon features. Its crystal structure is dominated by quasi-2D poly-oxoanions that correspond to unprecedented cutouts of the perovskite type of structure, where corner sharing (OsO₆) octahedra aggregate to form terraced slabs. The Os⁵⁺/Os⁶⁺ mixed valence oxide displays a particular charge ordering scheme. One osmium atom (Os1) per formula unit is in the valence state of 5+ in the whole temperature range studied, while the two remaining sites (Os2A and Os2B) show full charge disorder at high temperatures, resulting in an average charge of 5.5+. The latter, however, apparently undergo a process of continuous charge ordering at cooling. Full charge order appears to be established concomitantly with a phase transition to an antiferromagnetically ordered state at $T_{\text{(Néel)}} = 170$ K. This kind of temperature dependent continuous charge ordering is reflected by structural changes with temperature as well as by changes in paramagnetic response above $T_{\text{(Néel)}}$. Disentangling the intimate interplay between magnetic and charge ordering degrees of freedom will require applying sophisticated spectroscopy and (neutron) diffraction techniques.

Received 7th February 2018,

Accepted 25th March 2018

DOI: 10.1039/c8dt00528a

rsc.li/dalton

Introduction

Sr₂RuO₄ and Sr₂IrO₄, adopting the K₂NiF₄ type of structure, continue to be in the focus of solid state research as they represent prototypic systems displaying particular electronic structures giving rise to unconventional superconductivity in the ruthenate¹ or to a Mott insulating state in the strong spin-orbit interaction limit with a $J = \frac{1}{2}$ ground state in the iridate.² Against this background, it has been perceived as quite disturbing that the corresponding osmates have remained elusive. Sr₂OsO₄ and Ba₂OsO₄ are horizontal or vertical extrapolations in the periodic table of the respective ruthenates and iridates, and thus offer promising prospects for developing similar (exotic) electronic phases.

Alkaline earth oxido-osmates with osmium in octahedral coordination reported so far exhibit poly-oxoanions with various degrees of condensation of the primary OsO₆ building

units from monomeric (Ca₃LiOsO₆, Ba₁₁Os₄O₂₄, and Sr₁₁Os₄O₂₄),^{3–5} through chain-like Sr₂OsO₅⁶ to strands Sr₇Os₄O₁₉⁶ and finally 3D (perovskites: CaOsO₃, SrOsO₃, and BaOsO₃; weberites: Ca₂Os₂O₇ and Sr₂Os₂O_{7–x}).^{7–9} So far, no 2D layered alkaline earth oxido-osmates have been encountered.

Herein, we report on a first example of a 2D oxido-osmate anion, which, however, does not correspond to the planar tetragonal arrangement as found for the K₂NiF₄ type of structure, and further layered perovskite derivatives. Instead, strongly corrugated, less dense slabs are encountered. The title compound shows mixed valency with respect to osmium. Based on valence sums, calculated according to the bond length/bond strength concept,¹⁰ and calculations of the partial MAPLE values (MAPLE = Madelung Part of Lattice Energy),^{11–13} we suggest an assignment of oxidation states 5+ and 6+ to the respective Wyckoff sites. Crystal structure refinements on data collected at different temperatures have revealed a singular feature, namely, that the charge distribution varies continuously with temperature. This behavior is reflected by magnetic susceptibility, as well.

Experimental

Synthesis and crystal growth

Sr₅Os₃O₁₃ was synthesized as a polycrystalline powder by reacting stoichiometric amounts of SrO₂, SrO and OsO₂ at 1273 K

^aMax-Planck-Institut für Chemische Physik fester Stoffe, Nöthnitzer Straße 40, 01187 Dresden, Germany. E-mail: M.Jansen@jkf.mpg.de; Fax: +49 711 689 1502; Tel: +49 711 689 1501

^bMax-Planck-Institut für Festkörperforschung, Heisenbergstr. 1, 70569 Stuttgart, Germany

^cInstitut für Physik, Universität Augsburg, Universitätsstr. 1, D-86159 Augsburg, Germany

†Electronic supplementary information (ESI) available. See DOI: 10.1039/c8dt00528a



in an evacuated sealed quartz ampoule. SrO_2 (Sigma Aldrich, 99%) and SrO (Sigma Aldrich, 99%) were used as received. Purchased OsO_2 (Alfa Aesar, 83% Os) was further oxidized by heating it at 723 K in an evacuated sealed quartz ampoule in the presence of, however, not in contact with, a stoichiometric amount of PbO_2 , to get highly pure OsO_2 . A typical synthesis batch consisted of a mixture of SrO_2 (196 mg), SrO (248 mg) and OsO_2 (547 mg). These oxides were ground thoroughly inside a glovebox and pressed into a pellet that was placed in a corundum container and finally sealed in an evacuated quartz ampoule of approximately 2 cm diameter and 15 cm length. Single phase polycrystalline $\text{Sr}_5\text{Os}_3\text{O}_{13}$ was obtained after 12 h of heating at 1273 K. The heating and cooling rates were kept at 100 K h^{-1} , throughout.

Single crystals of $\text{Sr}_5\text{Os}_3\text{O}_{13}$ were obtained from the same starting materials, while applying a substantially different procedure. A physical mixture of SrO_2 and SrO was placed in a corundum crucible, and OsO_2 in a separate one; both these crucibles were put on the top of each other in a quartz ampoule, which was subsequently evacuated and sealed. Using the same heating treatment as for the pellet (see above), high quality crystals were grown in the crucible containing the strontium oxides. Slow gas phase transport of osmium oxide was accomplished *via in situ* formed volatile OsO_4 . The reaction products were harvested and handled in a glove box. The black blocks of $\text{Sr}_5\text{Os}_3\text{O}_{13}$ obtained from the crystal growth experiment were collected and washed with ethanol several times.

Powder X-ray diffraction and X-ray single crystal structure determination

Laboratory powder X-ray diffraction (PXRD) (Fig. 1) studies at RT were performed using a HUBER G670 imaging plate Guinier camera with $\text{Cu-K}\alpha$ radiation ($\lambda = 1.5406 \text{ \AA}$), covering a 2θ range of 5–85 degrees. Rietveld refinements were carried out with the program TOPAS-4.2.0.2 (AXS).¹⁴ The refined para-

meters were scale factor, zero point of θ , sample displacement (mm), background as a Chebychev polynomial of 20th degree and $1/x$ function, crystallite sizes, micro-strains, cell constants, atomic coordinates and thermal parameters; for more details, see the ESI (Tables SI-1 and SI-2†).

Crystals of $\text{Sr}_5\text{Os}_3\text{O}_{13}$, suitable for single-crystal X-ray diffraction, were selected and mounted on a thin glass fiber. Diffraction data were collected at 295, 200, 100 and 50 K using a Bruker SMART APEX-II CCD X-ray diffractometer (Bruker AXS, Karlsruhe, Germany), equipped with an N-Helix low-temperature device (Oxford Cryosystems, United Kingdom).¹⁵ The high temperature measurement at 500 K was performed on another crystal using a SMART APEX-I diffractometer (Bruker AXS, Karlsruhe, Germany) with a Cryostream700^{Plus} cooling device (Oxford Cryosystems, Oxford, United Kingdom, 80–500 K). Both diffractometers used $\text{Mo-K}\alpha$ radiation. The reflection intensities were integrated with the SAINT subprogram in the Bruker Suite software package,¹⁶ and a multi-scan absorption correction was applied using SADABS.¹⁷ The crystal structures of $\text{Sr}_5\text{Os}_3\text{O}_{13}$, at different temperatures, were solved by direct methods and refined by full-matrix least-squares fitting using the SHELXTL software package.^{18,19} The crystal data, and details of data collections and refinements are given in Table 1. Table 2 shows atomic coordinates and isotropic displacement parameters obtained for the intensity data collected at 500 and 295 K. Further details of the crystal-structure investigations, performed at 500, 295, 200, 100, and 50 K, may be obtained from the Fachinformationzentrum Karlsruhe, D-76344 Eggenstein-Leopoldshafen, Germany, on quoting the depository numbers CSD 434110 to CSD 434114 (<http://www.fiz-karlsruhe.de>).

Determination of the true lattice basis was challenged by sets of extremely weak superstructure reflections. A first routine type data collection resulted in a unit cell with $a = 14.1830(5)$, $b = 7.0846(2)$, and $c = 5.54143(2) \text{ \AA}$, at room temperature (cell 1). However, the crystal structure refinement (space group $Pbam$) produces physically unreasonable anisotropic displacement parameters and implausible bond lengths. A second data collection applying longer exposure times indeed revealed commensurate superstructure reflections requiring doubling of the c -axis (new b -axis with setting cell 2 according to the transformation of lattice base vectors as $a_2, b_2, c_2 = a_1, 2c_1, b_1$; see Table 1). These weak superstructure reflections disappear upon heating, and the diffraction data, obtained at 500 K, can be indexed by using cell 1. The anisotropic displacement parameters obtained from the latter data set are high, but still physically meaningful (see Fig. 2(a)). The transformation of the atomic coordinates from cell 1 into cell 2 corresponds to $x_2, y_2, z_2 = x_1, \frac{1}{2}z_1, y_1$. Due to symmetry reduction, atomic positions referring to cell 1 split accordingly to x, y, z and $-x, y, -z$ (see Table 2, cell 1 and cell 2). The results of respective refinements based on cell 2 (space group $Pnma$) appear to be much more reliable for the room temperature data (see Fig. 2(b)). Nevertheless, there is still some peculiar anisotropic thermal motion of the oxygen atoms left, which cannot be resolved by further reducing symmetry (space

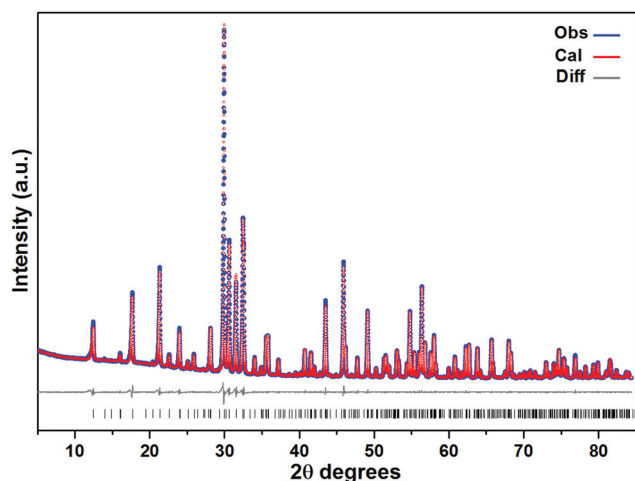


Fig. 1 A PXRD pattern of $\text{Sr}_5\text{Os}_3\text{O}_{13}$ (cell 2, see Table 1) at RT (blue spheres: observed; red spheres: fit from Rietveld refinement; gray line: difference curve; lower black bars: positions of Bragg peaks).



Table 1 Crystal data, data collection, and refinement details for Sr₅Os₃O₁₃

Temperature/K	500 Cell 1	295 Cell 2	100 Cell 2	50 Cell 2
Formula weight	1216.70			
Space group (no.), <i>Z</i>	<i>Pbam</i> (55), 2	<i>Pnma</i> (62), 4	<i>Pnma</i> (62), 4	<i>Pnma</i> (62), 4
Lattice parameters/Å	<i>a</i> = 14.2368(12) <i>b</i> = 7.0982(6) <i>c</i> = 5.5369(5)	14.1814(3) 11.0263(2) 7.0844(2)	14.1517(7) 10.9812(5) 7.0891(3)	14.1437(12) 10.9744(9) 7.0935(6)
<i>V</i> /Å ³	559.54(8)	1107.78(4)	1101.67(9)	1101.04(16)
$\rho_{\text{xray}}/\text{g cm}^{-3}$	7.222	7.295	7.336	7.340
Crystal size/mm ³	0.04 × 0.03 × 0.02	0.12 × 0.06 × 0.05	0.12 × 0.06 × 0.05	0.12 × 0.06 × 0.05
Diffractometer	SMART APEX I	SMART APEX II, Bruker AXS		
X-ray radiation, $\lambda/\text{Å}$	0.71073			
Absorption correction	Multi-scan, SADABS			
2 θ range/°	5.72 ≤ 2 θ ≤ 70.50	5.74 ≤ 2 θ ≤ 72.82	5.75 ≤ 2 θ ≤ 72.84	5.76 ≤ 2 θ ≤ 72.88
Index range	−22 ≤ <i>h</i> ≤ 23, −11 ≤ <i>k</i> ≤ 11, −8 ≤ <i>l</i> ≤ 8	−23 ≤ <i>h</i> ≤ 23, −18 ≤ <i>k</i> ≤ 18, −11 ≤ <i>l</i> ≤ 11	−23 ≤ <i>h</i> ≤ 23, −18 ≤ <i>k</i> ≤ 18, −11 ≤ <i>l</i> ≤ 11	−9 ≤ <i>h</i> ≤ 23, −16 ≤ <i>k</i> ≤ 17, −10 ≤ <i>l</i> ≤ 11
Reflections collected	8553	20 596	20 431	6808
Data, <i>R</i> _{int}	1328, 0.033	2811, 0.039	2796, 0.036	2653, 0.025
No. of parameters	62	110	110	110
Transmission: <i>t</i> _{min} , <i>t</i> _{max}	0.041, 0.110	0.003, 0.020	0.003, 0.020	0.004, 0.021
<i>R</i> ₁ [<i>F</i> ² > 2 σ (<i>F</i> ²)]	0.048	0.052	0.048	0.060
<i>wR</i> (<i>F</i> ²)	0.022	0.024	0.023	0.026
Extinction coefficient	0.00073(10)	0.00099(4)	0.00083(3)	0.00079(4)
CSD no.	434114	434113	434111	434110

Table 2 Atomic coordinates and displacement parameters *U*_{eq}(Å²) for Sr₅Os₃O₁₃, at 500 K (cell 1) and 295 K (cell 2)

Atom	Site	<i>x</i>	<i>y</i>	<i>z</i>	<i>U</i> _{eq}
Cell 1					
Os1	2 <i>a</i>	0	0	0	0.01183(7)
Os2	4 <i>h</i>	0.10918(2)	0.33251(3)	$\frac{1}{2}$	0.01376(6)
Sr1	2 <i>c</i>	0	$\frac{1}{2}$	0	0.0210(1)
Sr2	4 <i>h</i>	0.12391(5)	−0.17320(9)	$\frac{1}{2}$	0.0268(1)
Sr3	4 <i>g</i>	0.22585(4)	0.17024(8)	0	0.0192(1)
O1	2 <i>d</i>	0	$\frac{1}{2}$	$\frac{1}{2}$	0.0411(20)
O2	4 <i>h</i>	0.2063(4)	0.1611(9)	$\frac{1}{2}$	0.0428(14)
O3	4 <i>g</i>	0.1251(3)	−0.1211(6)	0	0.0247(9)
O4	8 <i>i</i>	0.0391(3)	0.1771(5)	0.2504(5)	0.0339(8)
O5	8 <i>i</i>	0.1599(3)	0.4734(6)	0.2482(5)	0.0350(9)
Cell 2					
Os1	4 <i>a</i>	0	0	0	0.00916(5)
Os2A	4 <i>c</i>	0.10925(2)	$\frac{1}{4}$	0.33953(3)	0.00995(5)
Os2B	4 <i>c</i>	−0.10899(2)	$\frac{3}{4}$	−0.32502(3)	0.01002(5)
Sr1	4 <i>b</i>	0	0	$\frac{1}{2}$	0.0151(1)
Sr2A	4 <i>c</i>	0.13030(4)	$\frac{1}{4}$	−0.17090(8)	0.0180(1)
Sr2B	4 <i>c</i>	−0.11820(4)	$\frac{3}{4}$	0.17622(8)	0.0167(1)
Sr3	8 <i>d</i>	0.22612(3)	0.00550(3)	0.16978(6)	0.01331(7)
O1	4 <i>c</i>	−0.0104(3)	$\frac{1}{4}$	0.4809(5)	0.0197(9)
O2A	4 <i>c</i>	0.2152(3)	$\frac{1}{4}$	0.1810(6)	0.0187(8)
O2B	4 <i>c</i>	−0.1990(4)	$\frac{3}{4}$	−0.1397(7)	0.0262(10)
O3	8 <i>d</i>	0.1248(2)	−0.0121(3)	−0.1219(5)	0.0165(6)
O4A	8 <i>d</i>	0.0490(2)	0.1226(3)	0.1702(5)	0.0233(7)
O4B	8 <i>d</i>	−0.0295(2)	0.1243(3)	−0.1844(5)	0.0224(7)
O5A	8 <i>d</i>	0.1531(2)	0.1243(3)	0.4938(5)	0.0201(6)
O5B	8 <i>d</i>	−0.1669(2)	0.1238(3)	−0.4517(5)	0.0209(6)

group *Pn2₁a*), considering twinning or not. For this reason, and because a pronounced feature in magnetic susceptibility evolves at ~170 K, further data collections were performed at 200, 100 and 50 K. Careful analyses of the diffraction data revealed a second set of very few and extremely weak

additional scattering features, which would require to approximately tri- or quadruplicate the *c*-axis, with respect to cell 2. Unfortunately, the diffuseness of these reflections did not allow their inclusion in a refinement of a commensurate lattice. Even so, neglecting this diffuse scattering has resulted in a reasonable crystal structure refinement with physically meaningful anisotropic displacement parameters throughout, and no further splitting of atomic sites was observed down to 50 K (see Table 2 and Fig. 2(c)).

Physical characterization

Thermogravimetric (TGA) analysis of Sr₅Os₃O₁₃ was carried out on a Netzsch STA 449 C analyzer. The sample (~20 mg) was placed in a corundum crucible, which was heated and subsequently cooled at a rate of 5 K min^{−1} in the range of 25–1000 °C under dynamic Argon flow.

Magnetization was measured in fields up to $\mu_0 H = 7$ T using a MPMS-XL7 magnetometer (Quantum Design). The susceptibility of Sr₅Os₃O₁₃ was slightly dependent on fields, indicating the presence of ferromagnetic impurity. The data were corrected applying the Honda–Owen approach (extrapolation of $\chi(1/H)$ to 0). Electrical resistivity was determined on powders pressed in a sapphire die cell with Pt contacts using the van der Pauw method and direct current. Heat capacity was measured by a relaxation method (HC option, PPMS, Quantum Design).

Results and discussion

Synthesis and chemical properties

Black, air-stable microcrystalline powders and single crystals of new Sr₅Os₃O₁₃ were obtained from stoichiometric amounts



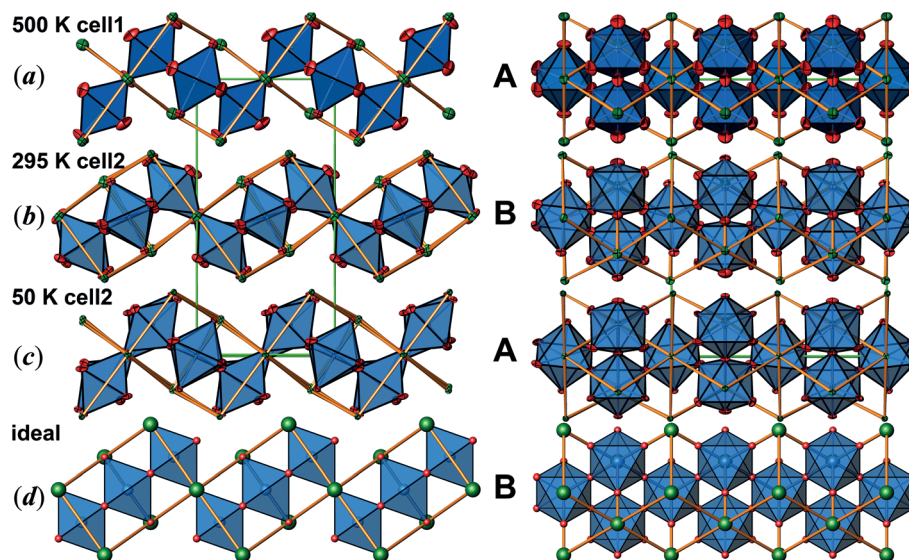


Fig. 2 The crystal structure of $\text{Sr}_5\text{Os}_3\text{O}_{13}$, left: view along $[0\ 1\ 0]$, right: view along $[0\ 0\ 1]$, with respect to cell 2. Displacement parameters (75% probability) displayed in different layers correspond to the different temperatures given [(a)–(c)]. Slab (d) shows a respective cutout of an ideal, undistorted perovskite structure. The stacking sequence of differently oriented layers is labeled with A and B. Color code: blue, octahedra (OsO_6); red, ellipsoids (O); blue, ellipsoids (Os); green, ellipsoids (Sr); orange sticks, shortest Sr–Sr distances; green sticks, margin of the unit cell 2.

of binary reactants by solid-state reactions in an evacuated sealed quartz ampoule. According to the standard oxidation states of Sr^{2+} and O^{2-} , and the requirement for charge neutrality, the new osmate shows mixed-valency with an average oxidation number of 5.33+ for osmium. According to TGA, the title compound is at least stable up to 800 °C; for the figure of TGA/DTA, see the ESI (Fig. SI-1†).

Crystal structure description

The crystal structure of $\text{Sr}_5\text{Os}_3\text{O}_{13}$ was determined from single-crystal X-ray diffraction data, collected at 500, 295, 200, 100, and 50 K. A structural phase transition was observed to occur in the temperature range of 295–500 K. $\text{Sr}_5\text{Os}_3\text{O}_{13}$ adopts two closely related crystal structures: (1) space group $Pnma$ (no. 62), Pearson code $oP84$, $Z = 4$ at room temperature and below, and (2) space group $Pbam$ (no. 55), Pearson code $oP42$, $Z = 2$ at 500 K.

Osmium is in approximately octahedral coordination by oxygen. The primary building units OsO_6 are linked *via* common vertices, engaging three each from the Os2A and Os2B, and four from the Os1 centered coordination polyhedra, to form plate-like poly-oxoanions of composition Os_3O_{13} , extending parallel to (001) (see Fig. 2 and 3). The local connectivity pattern is visualized in Fig. 4. Interestingly, the resulting anionic partial structure corresponds to a slab excised from the perovskite structure; however, in contrast to known perovskite related layered structures, as represented by *e.g.* Sr_2RuO_4 ,²⁰ $\text{Sr}_3\text{Ru}_2\text{O}_7$,²⁰ and $\text{Sr}_4\text{Rh}_3\text{O}_{10}$,²¹ the poly-anion is not planar, but terraced (see Fig. 2 and 3). The height of the stages equals the length of one OsO_6 octahedron. The similarity to the perovskite pattern even comprises the strontium atoms, as

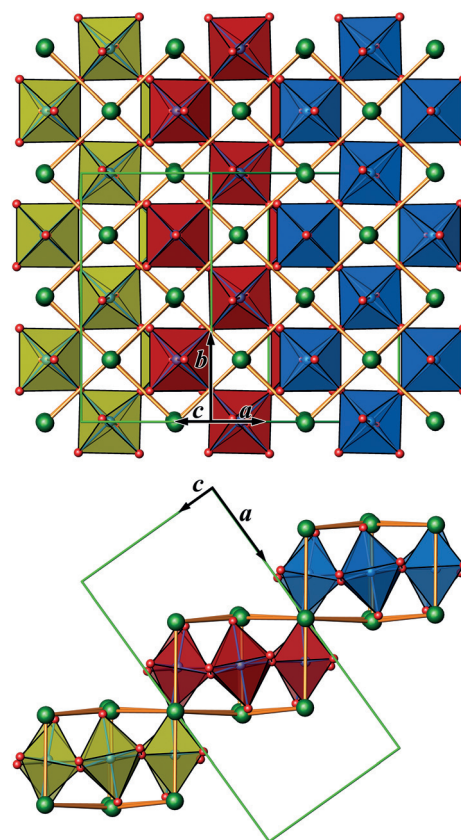


Fig. 3 Details of the crystal structure of $\text{Sr}_5\text{Os}_3\text{O}_{13}$ at 295 K, showing one octahedral layer along different directions of view. The differently colored polyhedra (yellow, red, and blue) emphasize OsO_6 octahedra of different heights (steps of a staircase). Atoms with the same color code as in Fig. 2.



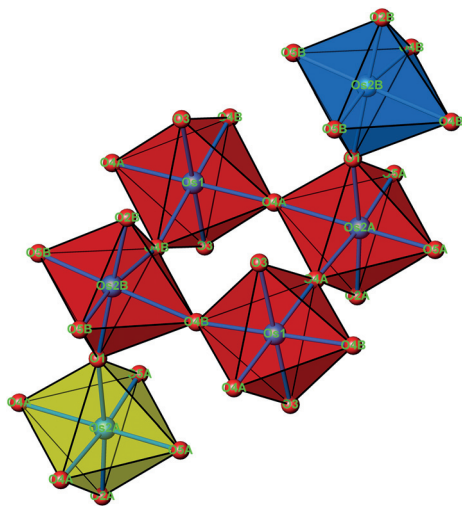


Fig. 4 A cutout of the crystal structure of $\text{Sr}_5\text{Os}_3\text{O}_{13}$, emphasizing the connectivity pattern of the OsO_6 octahedra. The same color code as in Fig. 3.

is highlighted schematically in Fig. 2(d) and 5. The mutual orientation of the layered $\text{Sr}_5\text{Os}_3\text{O}_{13}$ assemblies, however, does not follow the periodicity of the basic perovskite structure; by contrast, adjacent slabs are related by a $(0\bar{1}1)$ symmetry operation, which follows the descriptive approach of “chemical twinning”.^{22,23} The composition of the title compound can be easily rationalized considering the connectivity pattern as described: cleaving a regular “ $\text{Sr}_3\text{Os}_3\text{O}_9$ ” perovskite to generate the linkages of OsO_6 octahedra as encountered in the title compound and completing all coordination polyhedra of osmium would leave eight oxygen atoms per formula unit in a non-bridging function. Thus, four (or 8/2) more oxygen atoms are required, while interrupting part of the strontium sublattice entails inserting two more Sr atoms; taken together, this results in a composition of $\text{Sr}_5\text{Os}_3\text{O}_{13}$.

In Fig. 2, we illustrate the structural changes occurring along with charge ordering. The phase transition proceeds diffusionless, and the structural relaxation mainly consists of slight shifts of the oxygen atoms, resulting in combined tilting and breathing motions of the OsO_6 octahedra. The slabs

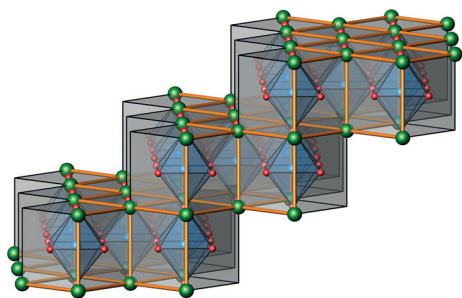


Fig. 5 A perspective view of a cutout of an ideal, undistorted perovskite structure, emphasizing the “staircase-like” topology of one $\text{Sr}_5\text{Os}_3\text{O}_{13}$ layer; see also Fig. 2(d).

labelled (a), (b), and (c) represent the refinement results obtained at 500 K, 295 K, and 50 K, respectively. The amplitudes of anisotropic thermal motion of the oxygen atoms are large at 500 K (cell 1), while the structure “locks in” at lower temperatures ((b) and (c) in Fig. 2). Front and back stacked octahedra are no longer superimposed, meaning that the octahedra are slightly rotated around the b -axis (viewing direction, Fig. 2, left). In addition, they slightly turn out of the a - c plane. The reorientation pattern of the corner-sharing OsO_6 octahedra thus corresponds to a two-tilt system with rotations of about $\pm 5^\circ$ in both directions.

From the overall composition follows that the title compound is mixed-valent with respect to osmium. Formally, two distributions of oxidation states would apply, $2 \times \text{Os}^{5+}/1 \times \text{Os}^{4+}$ or $2 \times \text{Os}^{5+}/1 \times \text{Os}^{6+}$, where the latter appears to be more plausible because of the smaller spread of charges. In general, metal oxygen bond lengths would allow for suggesting a charge distribution. However, in the present case, the varying numbers of coordinating oxygen atoms in different structural functions—bridging or terminal—obscure the effect of charge differences among the osmium atoms. Moreover, the ionic radii²⁴ for Os^{5+} and Os^{6+} differ by just 0.03 Å for coordination number VI. Still, the average Os–O bond lengths (50 K data), amounting to 1.96, 1.95, and 1.92 Å for Os1, Os2A, and Os2B, respectively, are in the same range as reported in the literature,^{6–9} and comply with the sum of the ionic radii.²⁴ However, based on atomic distances (Table 3) alone it does not appear possible to assign oxidation states to individual osmium sites.

Calculations based on the MAPLE concept^{11–13} have proved to be a valuable tool for tracking charge distributions on a semi-quantitative level, and, moreover, for checking structure models for electrostatic reasonability. A structure model of *e.g.* a ternary oxide is considered as electrostatically consistent if the sum of MAPLE values of the respective binary constituents deviates from the MAPLE value of the ternary by less than 1%. Based on this well-confirmed observation, MAPLE values even for hypothetical binary oxides can be extracted from well characterised, electrostatically consistent compounds. For assessing the title compound, reference values for the hypothetical polymeric oxides “ OsO_3 ” and “ Os_2O_5 ” were obtained according to the equations $[\text{MAPLE}(\text{“OsO}_3\text{”}) = \text{MAPLE}(\text{Na}_2\text{OsO}_4) - \text{MAPLE}(\text{Na}_2\text{O})]$ and $[\text{MAPLE}(\text{“Os}_2\text{O}_5\text{”}) = \text{MAPLE}(\text{Ca}_2\text{Os}_2\text{O}_7) - 2\text{MAPLE}(\text{CaO})]$ from published experimental data.^{25–29}

The results of our calculations confirm that the structure models are electrostatically consistent within the framework of the MAPLE concept (Table 4). Furthermore, the assignment of charges to atomic positions has been evaluated by considering their partial MAPLE* values and comparing those with typical values found for reference materials. According to examples taken from the literature, Os(IV) ions exhibit average MAPLE values of 2048 kcal mol^{−1}, Os(V) average MAPLE of 2995 kcal mol^{−1} and Os(VI) ions average MAPLE of 3996 kcal mol^{−1}. The respective charge-independent MAPLE* values ($\text{MAPLE}^* = \text{MAPLE}/\text{charge}^2$) average to 118.5 kcal mol^{−1}. Performing MAPLE calculations on the aforementioned scenarios of



Table 3 Selected interatomic distances (Å) and angles (°) for Sr₅Os₃O₁₃, at 500, 295 and 50 K

Atomic contact		Distance @500 K	Multi.	Distance @295 K	Multi.	Distance @50 K	Multi.
Os1 C.N. 6	–O4A	1.953(3)	×4	1.940(3)	×2	1.935(4)	×2
	–O4B	—		1.965(3)	×2	1.970(4)	×2
	–O3	1.977(4)	×2	1.974(3)	×2	1.981(4)	×2
Os2A C.N. 6	–O5A	1.862(3)	×2	1.871(3)	×2	1.879(4)	×2
	–O2A	1.841(5)	×1	1.876(4)	×1	1.897(5)	×1
	–O1	1.957(1)	×1	1.971(4)	×1	1.984(5)	×1
Os2B C.N. 6	–O4A	2.030(3)	×2	2.035(3)	×2	2.020(4)	×2
	–O2B	—		1.831(5)	×1	1.842(5)	×1
	–O5B	—		1.848(3)	×2	1.835(4)	×2
Sr1 C.N. 12	–O1	—		1.961(4)	×1	1.961(5)	×1
	–O4B	—		2.021(3)	×2	2.010(4)	×2
	–O5A	2.666(4)	×4	2.567(3)	×2	2.547(4)	×2
Sr2A C.N. 11	–O4B	2.736(4)	×4	2.674(4)	×2	2.679(4)	×2
	–O5B	—		2.754(3)	×2	2.741(4)	×2
	–O1	2.769(1)	×2	2.764(1)	×2	2.754(1)	×2
Sr2B C.N. 11	–O4A	—		2.788(4)	×2	2.807(5)	×2
	–O3	3.226(4)	×2	3.213(3)	×2	3.200(4)	×2
	–O4B	2.701(4)	×2	2.640(3)	×2	2.627(4)	×2
Sr3 C.N. 10	–O2B	2.647(7)	×1	2.768(5)	×1	2.734(5)	×1
	–O2A	2.689(7)	×1	2.769(5)	×1	2.810(5)	×1
	–O5A	2.915(4)	×2	2.769(4)	×2	2.750(4)	×2
Os2A C.N. 6	–O3	2.793(1)	×2	2.912(3)	×2	2.913(4)	×2
	–O4A	3.090(4)	×2	3.023(4)	×2	3.024(5)	×2
	–O1	2.915(1)	×1	3.173(5)	×1	3.198(5)	×1
Os2B C.N. 6	–O2B	—		2.514(5)	×1	2.495(5)	×1
	–O2A	—		2.570(4)	×1	2.545(5)	×1
	–O1	—		2.645(5)	×1	2.624(5)	×1
Sr3 C.N. 10	–O3	—		2.653(3)	×2	2.621(3)	×2
	–O4A	—		2.756(3)	×2	2.761(4)	×2
	–O5B	—		3.060(3)	×2	3.112(4)	×2
Os2A C.N. 6	–O4B	—		3.152(4)	×2	3.118(4)	×2
	–O3	2.517(5)	×1	2.525(3)	×1	2.527(4)	×1
	–O5B	2.547(3)	×2	2.528(3)	×1	2.517(4)	×1
Os2B C.N. 6	–O5A	—		2.557(3)	×1	2.544(4)	×1
	–O3	2.589(4)	×1	2.589(3)	×1	2.571(4)	×1
	–O5B	2.721(4)	×2	2.594(3)	×1	2.590(4)	×1
Os2A C.N. 6	–O2A	2.783(1)	×2	2.702(1)	×1	2.681(1)	×1
	–O4A	2.999(4)	×2	2.825(3)	×1	2.795(4)	×1
	–O5A	—		2.839(3)	×1	2.850(4)	×1
Os2B C.N. 6	–O2B	—		2.851(1)	×1	2.843(1)	×1
	–O4B	—		3.152(3)	×1	3.163(4)	×1
Angle		Degree @500 K	Multi.	Degree @295 K	Multi.	Degree @50 K	Multi.
Os2A–O1–Os2B		180	×1	166.0(3)	×1	164.2(3)	×1
Os1–O4A–Os2A		166.7(2)	×1	176.0(2)	×1	177.5(2)	×1
Os1–O4B–Os2B		—		157.6(1)	×1	157.3(2)	×1

Table 4 Results of the MAPLE calculations for Sr₅Os₃O₁₃ presenting the total MAPLE and the charge distribution (charge-corrected MAPLE*) yielding the best fit compared with the MAPLE calculations on SrO,²⁵ Na₂OsO₄,²⁶ Na₂O,²⁷ Ca₂Os₂O₇,²⁸ and CaO²⁹

	50 K	100 K	200 K	295 K	500 K
MAPLE (Sr ₅ Os ₃ O ₁₃)	82 901 kJ mol ^{−1} (Δ = 0.29%)	82 984 kJ mol ^{−1} (Δ = 0.30%)	82 828 kJ mol ^{−1} (Δ = 0.38%)	82 669 kJ mol ^{−1} (Δ = 0.57%)	82 746 kJ mol ^{−1} (Δ = 0.48%)
Os1	+5 (116.6)	+5 (116.6)	+5 (117.0)	+5 (117.1)	+5 (117.1)
Os2A	≈5 (119.6)	≈5 (119.8)	+5 ₂ (117.0)	+5 ₂ (117.2)	+5 ₂ (118.6)
Os2B	≈6 (117.3)	≈6 (117.1)	+5 ₂ (119.6)	+5 ₂ (119.4)	
rms dev. (MAPLE*)	0.8	0.9	0.8	0.7	0.5
5MAPLE(SrO) + MAPLE(“Os ₂ O ₅ ”) + MAPLE(“OsO ₃ ”)	83 144 kJ mol ^{−1}				



charge distributions over the three osmium sites indicated a more pronounced differentiation in charges in the sense of enhanced charge ordering below 200 K compared to the structure models refined using the 295 and 500 K data, respectively (Table 4). Taking into account all these factors we conclude that Os1 carries a formal charge of +5 within the full temperature range studied. The atomic parameters resulting from refinements based on intensity data collected at 200, 295 and 500 K reflect an equal charge distribution on osmium sites Os2A, Os2B, and Os2, respectively, where an average charge of +5.5 yields the best charge distribution model. At 50 and 100 K, Os2A and Os2B apparently “disproportionate”, with Os2B approaching +6 and Os2A +5. Even considering the limitations of the MAPLE concept and the slight deficiency in the crystal structure determination, these results suggest assigning an oxidation state of 5+ to Os1 below and above $T_{\text{Néel}}$, while for Os2A and Os2B 5+/6+ charge disorder prevails above. Below ~150 K, clear signatures for charge ordering into 6+ for Os2B and 5+ for Os2A have been obtained. The bond valence sums calculated are in correspondence with these assignments, resulting in BVS of 4.97, 5.17 and 5.97 for Os1, Os2B and Os2A, respectively (Table SI-3a, b and c†).

Magnetic and thermal properties

The thermally quite stable title compound, $\text{Sr}_5\text{Os}_3\text{O}_{13}$, is a semiconductor displaying a resistivity of about 10 Ωcm under ambient conditions and a significant band gap of approximately $E_a = 130$ meV as obtained from an Arrhenius type fit of the high temperature regime only. The full range temperature dependence of electronic conductivity can be fairly fitted by applying the variable range hopping model (see Fig. 6). Against this background, it appears adequate to analyse the magnetic properties in terms of basically localized magnetic moments. The $\chi(T)$ trace (Fig. 7) shows a pronounced indication for the onset of antiferromagnetic (afm) ordering at

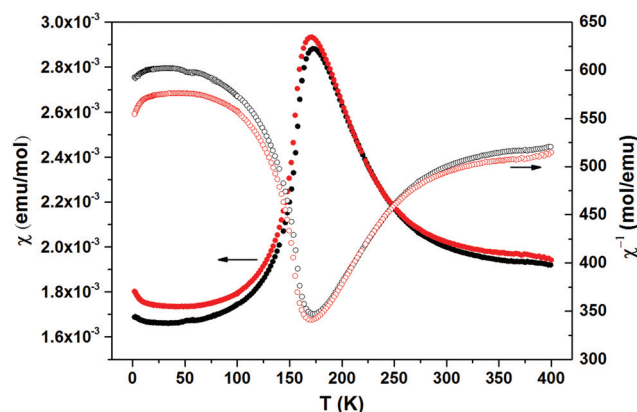


Fig. 7 Temperature dependence of the magnetic susceptibility χ (spheres) and of the inverse magnetic susceptibility χ^{-1} (circles) for $\text{Sr}_5\text{Os}_3\text{O}_{13}$ measured in magnetic fields of $\mu_0 H = 3.5$ T (red, cooling mode) and 7.0 T (black, warming mode).

$T_{\text{Néel}} = 170$ K, which is reflected by a respective feature in the specific heat (Fig. 8), as well. However, the paramagnetic branch of $\chi(T)$ above T_N shows an atypical behavior. Falling below the expected hyperbolic trend, the paramagnetic response appears to be suppressed, and only above about ~340 K it approaches values and a track that would allow one to apply the Curie–Weiss law. This observation suggests that on average the contributing local magnetic moments vary with temperature, which would parallel the continuous process of charge ordering as observed *via* the structural evolution with temperature. For an apparently concomitant evolution of the magnetic ground state with temperature we see three possible explanations: (1) the temperature dependent charge distribution is not restricted to a fixed ratio of Os^{5+} and Os^{6+} , but may include varying shares of Os^{4+} , (2) the splitting of d states as affected by a ligand field, spin–orbit coupling and Hund’s

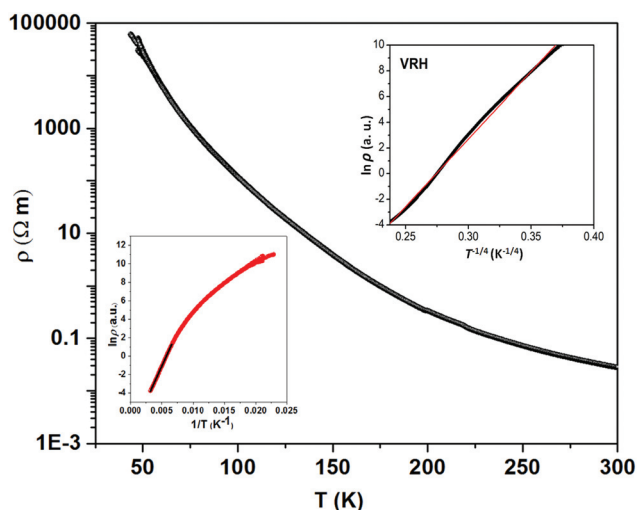


Fig. 6 Temperature dependence of the electric resistivity of polycrystalline $\text{Sr}_5\text{Os}_3\text{O}_{13}$. The insets show the Arrhenius plot (left bottom) and variable range hopping plot (right top) with the best-fit lines.

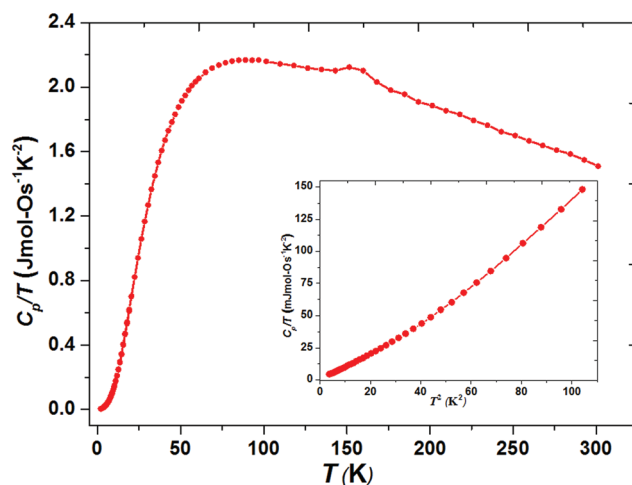


Fig. 8 Temperature dependence of specific heat divided by temperature, C_p/T , for $\text{Sr}_5\text{Os}_3\text{O}_{13}$. The specific heat data are per mol of Os. The inset shows the same data C_p/T as a function of T^2 for temperatures $T < 10$ K.



coupling varies with temperature or is in the range of kT , or (3) above $T_{\text{Néel}}$ a part of the afm coupling initially survives and fades away at increasing temperature. Based on the results of crystal structure analyses at different temperatures, we exclude scenario (1). From the $5d^3$ and $5d^2$ electron configurations of Os^{5+} and Os^{6+} , respectively, $t_{2g}^3e_g^0$ and $t_{2g}^2e_g^0$ based states would result in ideal octahedral coordination, where the t_{2g} levels on their part may split due to strong spin-orbit coupling into partly filled $j = 3/2$ and empty $j = 1/2$ shells, while alternatively for Os^{5+} , in the sense of a high spin arrangement, all t_{2g} orbitals can be occupied by a single electron, as well. Further considering the actually low symmetry of the ligand fields, it is obvious that the resulting term schemes will be quite complex, which would principally admit an explanation according to (2). From the crystal structure it is evident that there is a range of competing magnetic exchange paths, and thus magnetic ordering may occur at different temperatures for the different substructures, and thus explanation according to (3) may be valid as well. Evidently, for solving this puzzle, follow-up experimental studies are required, in the first place high resolution electron spectroscopy and neutron diffraction, which in addition would be quite suited to shed more light into the charge ordering processes.

Conclusions

$\text{Sr}_5\text{Os}_3\text{O}_{13}$, which was prepared by reacting the binary constituent oxides in sealed quartz ampoules, constitutes another member of perovskite derived multinary oxides. An $(\text{Os}_3\text{O}_{13})^{10-}$ polyanion evolves a singular connectivity pattern of octahedra, resulting in quasi-2D corrugated slabs. Similar to comparable multinary oxides of 5d transition elements, the electronic properties of the new mixed-valency oxide are controlled by an intricate interplay of the local effects of ligand field splitting, spin-orbit coupling and Hund's coupling, which are energetically in the same order of magnitude, and in addition by collective phenomena of charge, spin and orbital ordering. Noteworthy, the charge ordering within the title compound appears to occur over a wide temperature range, which is a rare observation. Against this background it is well understandable that complex ordering processes take place and that it is difficult to unambiguously reveal the electronic and magnetic groundstates. The qualitative explanations discussed need to be confirmed experimentally, using state of the art diffraction techniques and spectroscopy.

Conflicts of interest

There are no conflicts to declare.

Acknowledgements

We thank Dr. Walter Schnelle and Ralf Koban for performing magnetization, electronic conductivity and specific heat

measurements. Open Access funding provided by the Max Planck Society.

References

- (a) R. Matzdorf, Z. Fang, Ismail, J. Zhang, T. Kimura, Y. Tokura, K. Terakura and E. W. Plummer, *Science*, 2000, **289**, 746–748; (b) C. Bergemann, A. P. Mackenzie, S. R. Julian, D. Forsythe and E. Ohmichi, *Adv. Phys.*, 2003, **52**(7), 639–725; (c) C. Kallin, *Rep. Prog. Phys.*, 2012, **75**, 042501–042512.
- (a) I. V. Solovyev, V. V. Mazurenko and A. A. Katanin, *Phys. Rev. B: Condens. Matter Mater. Phys.*, 2015, **92**, 235109; (b) D. Proepper, A. N. Yaresko, M. Hoepfner, Y. Matiks, Y. L. Mathis, T. Takayama, A. Matsumoto, H. Takagi, B. Keimer and A. V. Boris, *Phys. Rev. B*, 2016, **94**, 035158; (c) S. D. Matteo and M. R. Norman, *Phys. Rev. B*, 2016, **94**, 075148.
- Y. Shi, Y. Guo, S. Yu, M. Arai, A. Sato, A. A. Belik, K. Yamaura and E. T. Muromachi, *J. Am. Chem. Soc.*, 2010, **132**, 8474–8483.
- M. Wakeshima and Y. Hinatsu, *Solid State Commun.*, 2005, **136**, 499–503.
- A. Tomaszewska and H. Muller-Buschbaum, *Z. Anorg. Allg. Chem.*, 1993, **419**, 1738–1742.
- S. A. Mohitkar, W. Schnelle, C. Felser and M. Jansen, *Inorg. Chem.*, 2016, **55**, 8201–8206.
- (a) R. F. Sarkozy and B. L. Chamberland, *Mater. Res. Bull.*, 1993, **8**, 1351–1360; (b) Y. Shi, Y. Guo, Y. Shirako, W. Yi, X. Wang, A. A. Belik, Y. Matsushita, H. L. Feng, Y. Tsujimoto, M. Arai, N. Wang, M. Akaogi and K. Yamaura, *J. Am. Chem. Soc.*, 2013, **135**, 16507–16516.
- J. Reading, C. S. Knee and M. T. Weller, *J. Mater. Chem.*, 2002, **12**, 2376–2382.
- I. S. Shaplygin and V. B. Lazarev, *Thermochim. Acta*, 1979, **33**, 225–229.
- (a) I. D. Brown and R. D. Shannon, *Acta Crystallogr., Sect. A: Found. Crystallogr.*, 1973, **29**, 266–282; (b) O. C. Gagne and F. C. Hawthorne, *Acta Crystallogr., Sect. B: Struct. Sci.*, 2015, **71**, 562–578.
- R. Hoppe, *Angew. Chem., Int. Ed. Engl.*, 1966, **5**, 95–106.
- R. Hoppe, *Angew. Chem., Int. Ed. Engl.*, 1970, **9**, 25–34.
- R. Hübenthal, *MAPLE, Program for the Calculation of the Madelung Part of Lattice Energy*, 1993.
- TOPAS-V4.2.0.2: *General Profile and Structure Analysis Software for Powder Diffraction Data*, Bruker AXSGmbH, Karlsruhe, Germany.
- G. Cakmak, J. Nuss and M. Jansen, $\text{LiB}_6\text{O}_9\text{F}$, the First Lithium Fluorooxoborate-Crystal Structure and Ionic Conductivity, *Z. Anorg. Allg. Chem.*, 2009, **635**, 631–636.
- Bruker Suite, version 2013/1*, Bruker AXS Inc., Madison, WI, 2013.
- G. M. Sheldrick, *SADABS —Bruker AXS area detector scaling and absorption, version 2012/1*, University of Göttingen, Germany, 2012.



- 18 G. M. Sheldrick, Short History of SHELX, *Acta Crystallogr., Sect. A: Found. Crystallogr.*, 2008, **64**, 112–122.
- 19 G. M. Sheldrick, Crystal Structure Refinement with SHELXL, *Acta Crystallogr., Sect. C: Struct. Chem.*, 2015, **71**, 3–8.
- 20 H. Müller-Buschbaum and J. Wilkers, *Z. Anorg. Allg. Chem.*, 1990, **591**, 161–166.
- 21 K. Yamaura, Q. Huang, D. P. Young and E. T. Muromachi, *Chem. Mater.*, 2004, **16**, 3428–3430.
- 22 B. G. Hyde and S. Andersson, *Inorganic Crystal Structures*, John Wiley & Sons, New York, 1989.
- 23 F. Zürcher, S. Wengert and R. Nesper, *Inorg. Chem.*, 1999, **38**, 4567–4569.
- 24 R. D. Shannon, *Acta Crystallogr., Sect. A: Cryst. Phys., Diffraction, Theor. Gen. Crystallogr.*, 1976, **32**, 751–767.
- 25 O. J. Rutt, G. R. Williams and S. J. Clarke, *Chem. Commun.*, 2006, 2869–2871.
- 26 S. F. Matar, G. Demazeau and N. Ouaini, *J. Solid State Chem.*, 2010, **183**, 402–407.
- 27 Yu. N. Zhuravlev and O. S. Obolonskaya, *Zh. Strukt. Khim.*, 2010, **51**, 1005–1013.
- 28 J. Reading, C. S. Knee and M. T. Weller, *J. Mater. Chem.*, 2002, **12**, 2376–2382.
- 29 Q. Huang, O. Chmaissem, J. J. Caponi, C. Chaillout, M. Marezio, J. L. Tholence and A. Santoro, *Physica C*, 1994, **227**, 1–9.

